Momentum-resolved photoelectron absorption in surface barrier scattering on Ir(111) and graphene/Ir(111)

A. Zaporozhchenko-Zymaková,[1,2] D. Kutnyakhov,[2,3] K. Medjanik,[2] C. Tusche,[4] O. Fedchenko,[2] S. Chernov,[2] M. Ellguth,[2] S. A. Nepijko,[2] H. J. Elmers,[1,2] and G. Schönhense[1,2]

[1]*Mainz Graduate School of Excellence, 55128 Mainz, Germany*

[2]*Institut für Physik, Johannes Gutenberg-Universität, 55128 Mainz, Germany*

[3]*DESY, 22607 Hamburg, Germany*

[4]*Forschungszentrum Jülich GmbH, Peter Grünberg-Institut, 52425 Jülich, Germany*

(Received 20 March 2017; revised manuscript received 17 August 2017; published 9 October 2017)

Time-of-flight momentum microscopy reveals sixfold symmetric sharp features of decreased intensity (dark lines) in constant-energy maps for clean Ir(111) and graphene/Ir(111). The dark lines have been observed for *p*- and *s*-polarized light in the photon-energy range of 20–27 eV and result from scattering of photoelectrons at the surface potential barrier. The phenomenon is strongly related to threshold effects in low-energy electron diffraction. A quantitative analysis of the dark lines' positions shows that the relevant reciprocal-lattice vector corresponds to the lattice of the topmost layer (in our case graphene and Ir, respectively). The dark lines appear in the momentum patterns only in a certain photon-energy range satisfying the additional condition that the electron wavelength matches the lattice periodicity.

DOI: 10.1103/PhysRevB.96.155108

I. INTRODUCTION

The surface of a crystal, breaking the translational symmetry of the three-dimensionally periodic potential inside the solid crystal, strongly changes the electronic states near the surface and therefore influences the interaction of any material with the environment. The precise spatial dependence of the surface potential barrier plays an important role for the occurrence of two-dimensional electronic surface states. Surface barrier scattering of photoelectrons with low kinetic energy provides a very efficient tool for the investigation of details of the surface potential barrier [1]. By measuring interference patterns for photoelectrons in the momentum domain, Winkelmann *et al.* [2] resolved specific quantum-mechanical effects of the surface barrier region of a Cu(001) surface.

While photoelectron interference observed for single-crystal surfaces is quite well understood, it remains an open question whether the reciprocal-lattice vector involved in the scattering process at heterogeneous surfaces comprising adsorbed monolayers is dominated by the substrate or by the adsorbate.

In order to answer this question, we compare a graphene layer grown on Ir(111) with the clean Ir(111) surface. Graphene, a two-dimensional honeycomb lattice of carbon atoms, has recently become one of the most intensely studied materials due to remarkable properties such as high thermal conductivity, optical transparency, mobility of electrons at the Fermi level, and Dirac massless fermions [3–5]. Numerous intriguing properties of graphene originate from its nontrivial electronic structure. The valence and conduction band is connected at the *K* points of the surface Brillouin zone (SBZ) forming six pairs of head-to-head cones in the (E,k_x,k_y) space with linear dispersion in the vicinity of Fermi energy level [6,7]. The graphene/Ir(111) system has an important characteristic: the Dirac points of graphene coincide with partial band gaps in the projected spectral density of Ir(111). Therefore, the particular electronic states of graphene are preserved in the proximity of the Fermi level [8,9].

In the present article we analyze interference patterns appearing as dark lines in the photoemission spectra observed for graphene on Ir(111) and for clean Ir(111) using time-of-flight (ToF) momentum microscopy [10]. These two samples are characterized by different topmost layers and, therefore, different surface barriers between the material and vacuum. ToF momentum microscopy is characterized by simultaneous acquisition of all photoelectrons in the full half space above the sample in an energy interval between the Fermi energy (E_F) and 4 eV below E_F. This data array comprises the full SBZ and energy range of interest without the need for sequential measurements or sample rotation.

The dark lines originate from a diffraction process occurring at the surface barrier between the material and vacuum. The phenomenon is strongly related to threshold effects in low-energy electron diffraction (LEED). Highly resolved LEED intensities showed rapid oscillations at the emergency threshold of a new reflex [11]. The oscillations were firstly explained by surface resonances [12]. However, the hypothesis was refuted by theoretical studies of Le Bossé *et al.* [13] and Gaubert *et al.* [14], who proved that interference between the barrier or bulk reflections and the second-order bulk reflected beams at the threshold result in a Rydberg-like series of fine structures. In the present study we focus on the comparison of the graphene/Ir(111) heterosystem with the clean Ir(111) surface, revealing the reciprocal-lattice vector relevant for the appearance of the dark lines.

II. EXPERIMENTAL DETAILS

Graphene on Ir(111) was grown in a dedicated preparation chamber. The initial cleaning process included ion sputtering and annealing at 1300 K in oxygen (5×10^{-8} mbar). The cycles were followed by flash-annealing up to 1500–1800 K; the base pressure was better than 5×10^{-10} mbar. A graphene layer was grown on the clean Ir(111) crystal surface by heating in ethylene at a partial pressure of 2×10^{-7} mbar with

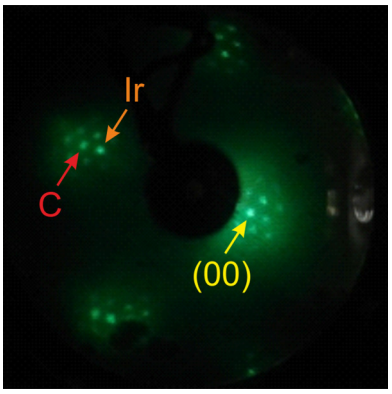

FIG. 1. LEED pattern of graphene/Ir(111).

heating up to 1520 K. The process is self-limiting, forming a single graphene layer [15]. Finally, the surface structure of the graphene/Ir(111) sample was checked by LEED (Fig. 1).

The mismatch of the lattice constants of graphene and Ir(111) leads to a regular Moiré-like superstructure of the graphene as investigated by scanning tunneling microscopy [15]. Several configurations of graphene on Ir(111) occur [16], which can also be distinguished by LEED [17]. In our case the diffraction pattern (Fig. 1) shows intense superstructure reflexes that are symmetrically placed around the specular beam (00) and all higher-order Ir(111) diffraction beams. Ir reflexes appear more intense. Direct comparison to different variants described in Ref. [17] reveals that in our case the graphene layer has been grown in the R_0 orientation. This is in accordance with the momentum patterns of our earlier study [10].

The photoemission experiments were performed at BESSY II, Helmholtz-Zentrum Berlin at beamline U125-2 NIM in 8-bunch mode [10] (measurements with p-polarized light) and single-bunch mode (measurements with s-polarized light). A sketch of the experimental geometry is shown in Fig. 2. The graphene/Ir(111) sample was illuminated at a shallow angle of 22°. Emitted electrons were recorded by the ToF k microscope with its optical axis oriented perpendicular to the surface. The data were measured in the range of excitation energies from 14 up to 23 eV for s polarization and up to 27 eV for p polarization. For the sake of direct comparison, all data sets were obtained at identical microscope settings.

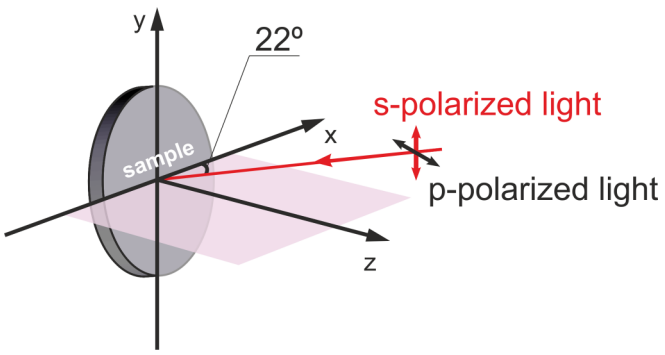

FIG. 2. Experimental geometry. For s-polarized light the electric vector points along the y axis; for p-polarized it lies in the x-z plane at 22° off the z axis.

The k microscope consists of three main parts—-the objective lens, the imaging column, and the field-free drift section (length 700 mm) for ToF parallel energy recording. In order to decouple momentum and energy coordinates the drift section is completely separated from the imaging column. Electron rays arising from different points of the sample at equal angles are collected in the back-focal plane of the objective lens and form the reciprocal, or Fourier image [18]. This is the fundamental principle of band-structure imaging using a momentum microscope.

A delay-line detector is mounted at the end of the ToF tube and serves as a time- and space-resolving detector. It consists of a multichannel-plate stack and two crossed delay lines. Each arriving electron is registered with its spatial coordinates k_x,k_y and its time of arrival at the detector surface with respect to the bunch marker of the photon beam [19]. The time of flight determines the kinetic energy of the electron, thus yielding the binding energy E_B by reference to E_F. More details on the method of momentum microscopy can be found in Ref. [20].

III. EXPERIMENTAL RESULTS

The complete 3D photoemission intensity array $I(E_B,k_x,k_y)$ of graphene/Ir(111) has been measured for excitation with p- and s-polarized synchrotron radiation at 10 different photon energies between $h\nu = 15$ and 27 eV. Figure 3 shows selected constant-energy cross sections of the data array acquired at $h\nu = 22$ eV. In order to eliminate part of the linear dichroism in the angular distribution [21] the sections were symmetrized according to the graphene symmetry. The sections display the flowerlike Ir $5d$ band augmented by the graphene π band [22]. At the Fermi level the graphene π band shows up as the six Dirac points with high intensity [Fig. 3(a)]. With increasing binding energy, the Dirac cones open with linear dispersion. At first the π band appears as circles, showing the previously observed dark corridors [19] that emerge as partially suppressed intensity [see Fig. 3(b)]. For higher binding energy, the π band exhibits six triangular-shaped features [Fig. 3(c)]. The data taken in this experiment complement data measured earlier with p-polarized light for an identical sample (see, for instance, Ref. [10]). The different photon polarization manifests in different relative intensities of the bands and the position of the dark corridors. We note that Fig. 3(c) clearly shows the hybridization of the graphene π band with the Ir d bands, visible at the inner basis of each triangle (oriented toward Γ); for details, see Ref. [10]).

The structures of interest for this study are the lines of decreased photoemission in the constant-energy maps within areas of otherwise homogeneous photoemission intensity. These dark lines are hardly visible in the constant-energy maps for graphene in Ir(111) as shown Fig. 3(a), and therefore green arrows and a dotted line indicate the position of the dark lines. In Figs. 3(b) and 3(c) the dark lines remain invisible, which can be explained by the smaller photoemission intensity and hence lower signal-to-noise ratio in the area where the dark lines are expected.

In order to enhance the visibility of the dark lines we adjust the contrast and brightness of the constant-energy and momentum sections largely overexposing the π-band related

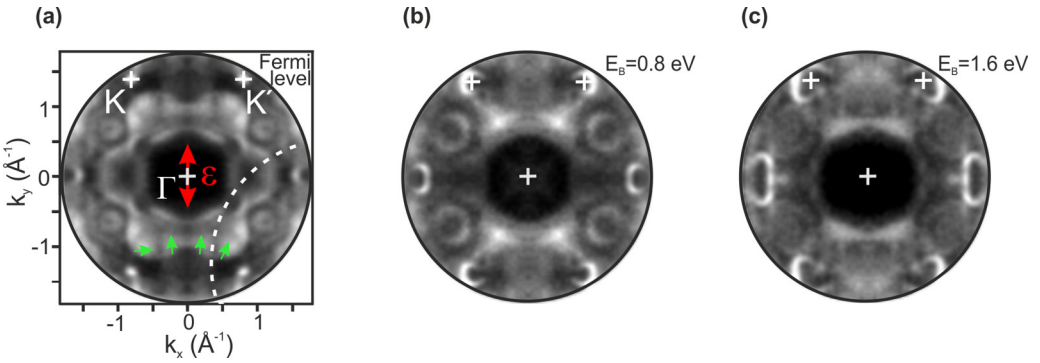

FIG. 3. (a)–(c) Constant-energy sections of the photoemission intensity array $I(E_B,k_x,k_y)$ for graphene/Ir(111) for three binding energies E_B, measured with s-polarized light. The red arrow in (a) indicates the orientation of the electric vector ε of the photon beam. White crosses denote K, K' and the center of the SBZ. All bands except the bright bands around K and K' originate from iridium. Dotted line indicates dark line.

features as shown in Fig. 4 for higher binding energies. At $E_B > 2$ eV the dark lines start crossing the most intense photoemission features of the graphene/Ir(111) sample. These features serve as a suitable background for visualization of the dark lines. At $E_B > 3$ eV the dark lines become fully visible [Figs. 4(d)–4(h)].

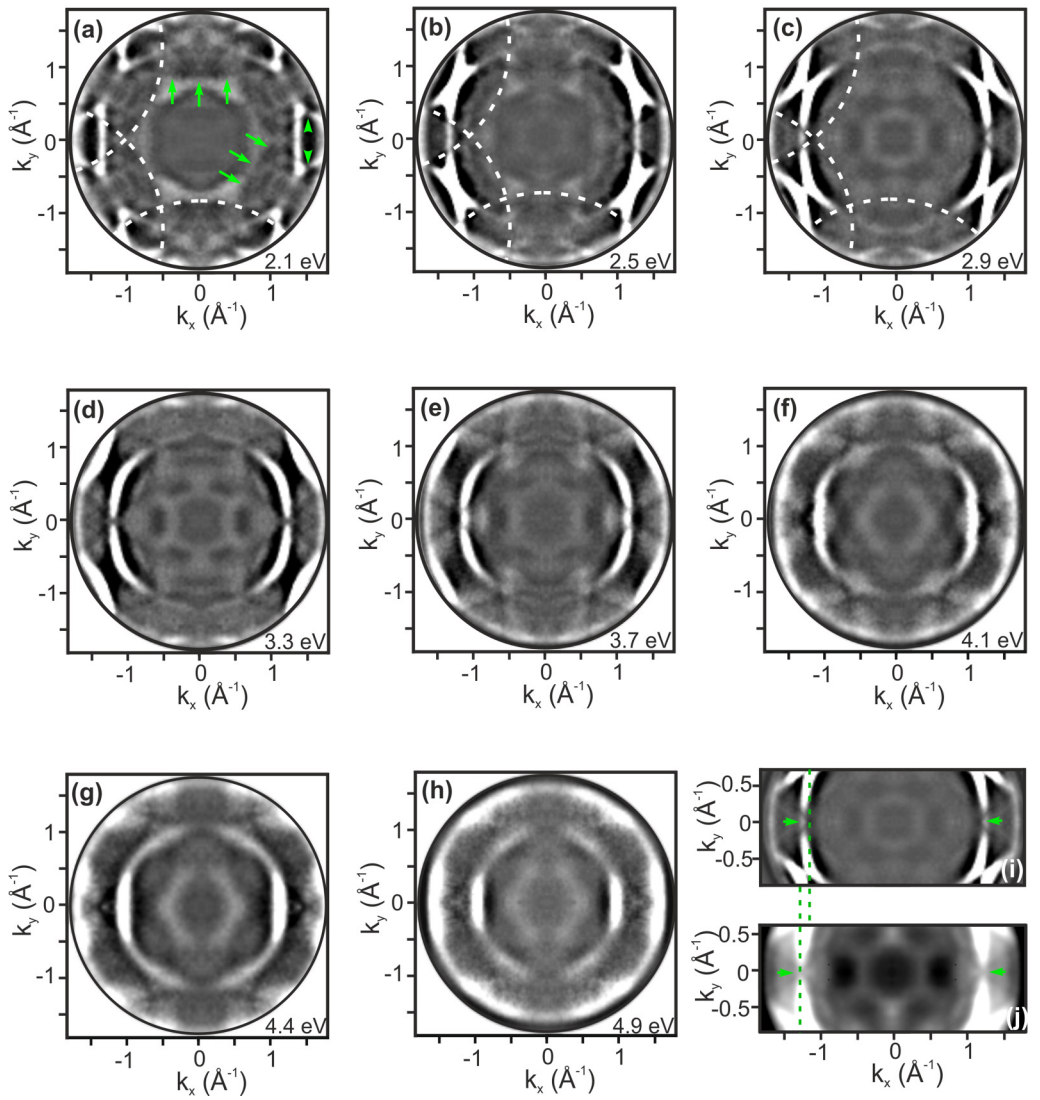

FIG. 4. Dark lines appearing in single isoenergetic slices at excitation energies of (a)–(i) $h\nu = 22$ eV; (j) $h\nu = 21$ eV. The binding energy E_B is noted in the bottom right corners. (i) and (j) show constant-energy slices at identical binding energies taken at different photon energies. Green arrows and dotted lines mark crossing points of dark lines, revealing a shift with photon energy.

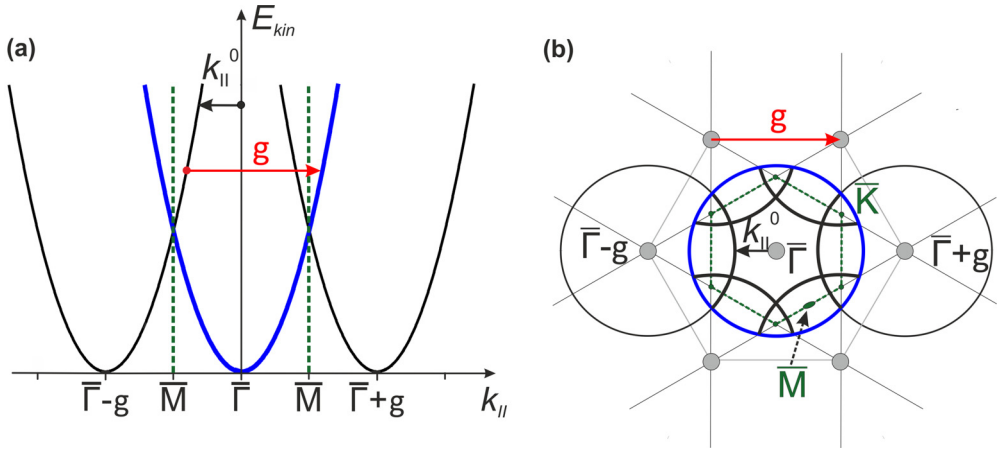

FIG. 5. Sketches in reciprocal space illustrating the formation of dark lines. (a) $E_B(k_{||})$ representation; the blue parabola marks the photoemission horizon, centered at $\bar{\Gamma}$ ($k_{||} = 0$). The red arrow connects two equivalent electron states $\hbar\boldsymbol{k}^0$ and $\hbar(\boldsymbol{k}^0 + \boldsymbol{g})$, with reciprocal-lattice vector $\boldsymbol{g}$. States positioned on the two black parabolas (denoting the photoemission horizons centered at $k_{||} = +/-g$) are translated by $\boldsymbol{g}$ onto states on the blue photoemission horizon. Hence in the $E_B(k_{||})$ scheme the black parabolas mark the positions of the dark lines in the observed patterns. (b) Same as in (a) but plotted as a constant-binding-energy slice in reciprocal space (k_x,k_y). The reciprocal-lattice points of the honeycomb structure are indicated by gray dots. The green dashed lines mark the first SBZ. Dark lines appear as section of the black circles centered at adjacent reciprocal-lattice points (at $k_{||} \neq 0$) with the area within the photoemission horizon of the first SBZ (blue circle).

The constant-energy maps in Fig. 4 reveal that the dark lines represent circular arcs. The arcs show a systematic shift to larger momentum values with increasing binding energy. The dark lines are relatively sharp compared to the band features originating from the graphene layer and the Ir surface. The suppression of the photoemission intensity due to the dark lines depends on the binding energy and on the photon energy, revealing a maximum visibility in the binding-energy range between 3.3 and 4.4 eV [Figs. 4(d)–4(g)] for a photon energy of 22 eV.

IV. DIFFRACTION MODEL

For a quantitative description of the dark-line positions, we extend the diffraction model given in Ref. [1] including a graphical representation of the effect.

In the photoemission process the transversal momentum of the escaping photoelectron is conserved since the surface barrier acts only on the perpendicular momentum. However, in addition elastic and inelastic scattering events occur. Within the lattice a state with momentum $\hbar\boldsymbol{k}$ is equivalent to a state with $\hbar(\boldsymbol{k} + \boldsymbol{g})$, where $\boldsymbol{g}$ is a reciprocal-lattice vector. After diffraction at the surface barrier, the kinetic energy for motion along the surface normal $E_\perp$ is given by [2]

$$E_\perp = E_{\rm kin} - E_\parallel = E_{\rm kin} - \frac{\hbar^2}{2m}|\boldsymbol{k}_\parallel + \boldsymbol{g}|^2 . \qquad (1)$$

$E_\perp$ equals zero for an electron traveling parallel to the surface, i.e., at the boundary of total reflection, leading to the kinetic energy of photoelectrons in this particular state:

$$E_{\rm kin} = \frac{\hbar^2}{2m}|\boldsymbol{k}_\parallel{}^0 + \boldsymbol{g}|^2 . \qquad (2)$$

$\boldsymbol{k}_{||}{}^0$ denotes a state positioned within the photoemission horizon but after addition of $\boldsymbol{g}$ is equivalent to a state right on the photoemission horizon within the next SBZ. The expected positions of the dark lines according to Eq. (2) are sketched in Fig. 5. Figure 5(a) shows the band dispersion $E_B(\boldsymbol{k}_{||})$ representation with the marked (blue) photoemission horizon, centered at $\bar{\Gamma}$ ($k_{||} = 0$). States positioned on the two parabolas centered at $\boldsymbol{k}_{||} = +/-\boldsymbol{g}$ are translated by $\boldsymbol{g}$ onto states on the photoemission horizon. Hence in the $E_B(\boldsymbol{k}_{||})$ representation the black parabolas mark the positions of the dark lines in the observed patterns. Figure 5(b) shows the corresponding constant-binding-energy slice in reciprocal space (k_x,k_y). The reciprocal-lattice points of the graphene or the topmost Iridium structure are indicated by gray dots. Dark lines appear as section of circles centered at adjacent reciprocal-lattice points (at $\boldsymbol{k}_{||} \neq 0$). The kinetic energy measured outside of the crystal follows from $E_{\rm kin} = h\nu - \Phi - E_B$ where Φ is the work function. Accordingly, at the Fermi level the kinetic energy can be expressed as $E_{\rm kin} = {\rm h}\nu\text{-}\Phi$.

The motion parallel to the surface results in emerging interference and absorption channels and hence to intensity oscillations starting at the threshold value $\boldsymbol{k}_{||}{}^0$ according to the energy condition, Eq. (2). At ideal surfaces the interaction of the electron with the surface is dominated by elastic scattering leading to characteristic interference patterns. In this case one expects a rapidly oscillating intensity as a function of E_B or $\boldsymbol{k}_{||}{}^0$ as discussed in Ref. [2]. In our case, we rather observe a decreased intensity for $\boldsymbol{k}_{||}{}^0$ leading to the dark lines. No signatures of an intensity increase or oscillations are visible in the data (see Figs. 4,5,7). We take this as a hint that in our case inelastic scattering is the dominant channel of the interaction. This might be attributed to scattering at residual gas adsorbates or surface defects.

In the following, we use the diffraction model based on Eqs. (1) and (2), sketched in Fig. 5, to intensify the visibility of the dark lines on the expense of the sharpness of band features. Figure 6 shows a collection of averaged momentum slices. Summing up rescaled slices in a binding-energy interval between the Fermi energy and $E_B = 3.5\,{\rm eV}$ reveals the

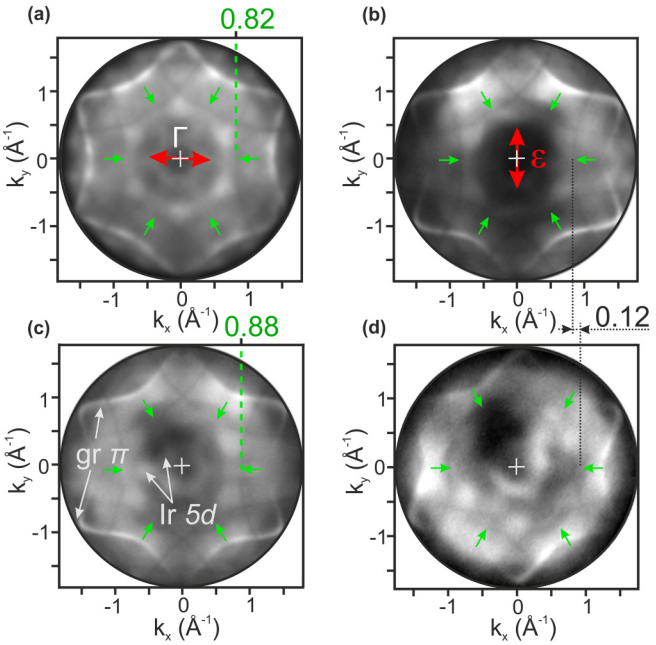

FIG. 6. Sum images of rescaled momentum sections of graphene/Ir(111) measured at (a) $h\nu = 22$ eV, p polarized; (b) $h\nu = 22$ eV, s polarized; (c) $h\nu = 21$ eV, s polarized; (d) $h\nu = 20$ eV, s polarized. Red arrows show the orientation of the electric vector $\boldsymbol{\varepsilon}$ of the photon beam [being out of plane for (a)]. Green arrows mark the dark lines. Dashed lines indicate the shift of the dark lines with increasing photon energy. The momentum scales correspond to the momentum section at the Fermi level. Dark areas in the central part in (c),(d) are experimental artifacts (defect on the image unit).

dark-line pattern with sixfold symmetry with good contrast. The averaging method exploits the fact that the dark lines exactly coincide with the (paraboloid-shaped) photoemission horizon of the first repeated SBZ. The corresponding outward dispersion (away from $k = 0$) with increasing binding energy has been compensated by rescaling each individual momentum slice by a factor proportional to $(X - E_B)^2$ [see Eq. (2)] before they were summed up. This procedure substantially reduces the statistical noise.

Six circularly shaped dark lines are now clearly observed within the first Brillouin zone, marked by green arrows. Each line is a section of a circle that extends beyond the field of view. The dark lines occur both for p- and s-polarized light in the same range of excitation energies. Please note that the Ir(111)- and graphene-related band features are partly blurred in the sum image due to their different dispersion relations. The graphene π band appears in this projected image as a sixfold star, confined at its inside by a circle. Ir bands appear mainly inside and outside of this star as marked in Fig. 6(c).

With increasing photon energy the position of the dark lines in k space moves toward smaller k values [see comparison in Figs. 6(a), 6(c) and 6(b), 6(d)]. At 22 eV the dark line appears at $k_x = 0.82\,\text{Å}^{-1}$, whereas at 21 eV its position is shifted by $0.06\,\text{Å}^{-1}$ away from the center of the SBZ.

The evaluation of the corresponding spectral functions $I(E_B,k_x,k_y)$ for the clean Ir(111) surface, measured with

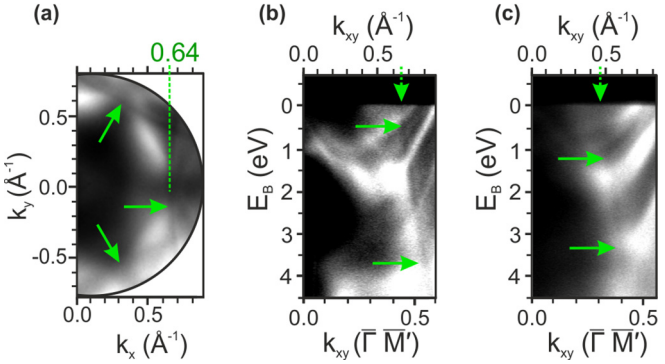

FIG. 7. Sections through the measured spectral density function of Ir(111) depicted as sum image of rescaled momentum sections (a) measured at a photon energy of $h\nu = 23$ eV and as E_B vs k sections measured at (b) $h\nu = 23$ eV and (c) $h\nu = 27$ eV. Green arrows mark the positions of the dark lines. The dashed vertical line indicates the position of one of the dark lines. As in Fig. 6, the momentum scale in (a) corresponds to the momentum section at the Fermi level.

p-polarized light, also reveals the occurrence of dark lines. A selection of sections is shown in Fig. 7.

In order to confirm the proposed model quantitatively, we compare the measured positions of the dark-line reciprocal-lattice vector resulting from Eq. 2 for clean Ir(111) and graphene/Ir(111) measured at several photon energies with the corresponding literature values from structural investigations. From the lattice constants of graphene and Ir in real space (2.46 Å [23] and 2.71 Å [24], respectively) we calculate the lengths $g_{\text{graphene}} = 2.95\,\text{Å}^{-1}$ and $g_{\text{Ir}} = 2.68\,\text{Å}^{-1}$. Evaluation of the data shown in Fig. 6 reveals an experimental value $g_{\text{graphene}} = 2.92(3)\,\text{Å}^{-1}$, which is in good agreement with the structural data of graphene. For the case of clean Ir the reciprocal-lattice constant obtained from the position of the dark lines is $g_{\text{Ir}} = 2.74(6)\,\text{Å}^{-1}$, which agrees with the expected value within the error bar. We conclude that in both cases, graphene/Ir and clean Ir, the reciprocal-lattice vector of the topmost layer determines the position of the dark lines, i.e., the underlying process happens at the very surface.

Table I summarizes the dark-line positions as measured and calculated from the lattice constants. The work functions of clean Ir and graphene/Ir are assumed to be 6 and 5 eV, respectively. The uncertainty in the evaluation of the dark-line position is 4% in the case of graphene/Ir(111) and larger (13%) in the case of clean Ir(111) because of the smaller intensity variation.

Intensity profiles across the dark lines (not shown here) reveal an intensity decrease with a full width at half maximum of less than $0.03\,\text{Å}^{-1}$. This value corresponds to the momentum resolution of the present experiment.

The experimental data shown in Figs. 7(b) and 7(c) indicate that dark lines can only be observed in a narrow interval of kinetic energies (the ranges of visibility are marked with green arrows). Similarly, in Fig. 6 it is clearly visible that the dark lines at E_F are pronounced at $h\nu = 22$ eV and appear much weaker at 20 eV. This means that the dark lines are visible for surface parallel momenta close to half of the first Brillouin-zone boundary, as we will analyze in the following.

TABLE I. Positions of dark lines at E_F along the $\overline{\Gamma M}$ direction as calculated from the lattice constant (columns 2 and 3) and measured (columns 4 and 5).

	Position from lattice constant ($Å^{-1}$)		Position from experiment ($Å^{-1}$)	
$h\nu$ (eV)	Ir(111) $g = 2.68$	Graphene/Ir(111) $g = 2.95$	Ir(111) $g = 2.74(6)$	Graphene/Ir(111) $g = 2.92(3)$
20	0.77	0.97	0.83(10)	0.94(3)
21	0.70	0.91	0.76(10)	0.88(3)
22	0.64	0.85	0.7(9)	0.81(3)
23	0.58	0.79	0.64(8)	0.76(3)
27	0.34	0.56	0.45(6)	0.53(2)

In an attempt to explain this observation, we consider two isoenergetic electronic states fulfilling the dark-line condition [Eq. (2)] that possess antiparallel momenta of $k_{||} = +/-0.25g$ (half of the BZ diameter). The corresponding wavelengths of their Bloch states electron density equal the doubled atomic distance in real space. The superposition of the two density waves traveling in opposite directions results in a standing wave where the distance of knots or bows, respectively, matches the atomic lattice. This lattice matching may provide a condition that enhances the scattering probability in analogy to a nesting phenomenon, where the nesting vector is given by the Brillouin-zone boundary.

The photoelectron diffraction effect discussed here differs both in appearance and in physical origin from previously reported interference features also showing up as momentum-dependent intensity reduction. The coherent electronic fringe structure observed in incommensurate silver-silicon quantum wells [25] shows a negative effective mass in contrast to the positive curvature observed in our case. The multitude of similar interference patterns in lattice-mismatched structures observed in Ref. [26] originates from replicated bands caused by the geometrical corrugation of the system. The small gaps in the graphene π band appearing as a result of the avoided-crossing effect observed in Ref. [27] also originate from periodically corrugated graphene on Ir(111).

V. CONCLUSIONS

We have presented a detailed investigation of three-dimensional photoelectron momentum distributions $I(E_B,k_x,k_y)$ revealing signatures of a photoelectron diffraction process for the graphene/Ir(111) and clean Ir(111) surface. For both surfaces sharp interference patterns appearing as dark lines occur in the constant-energy and constant-momentum sections. Following a model introduced in Ref. [2] these dark lines originate from an umklapp process involving a reciprocal-lattice vector. We find that the relevant reciprocal-lattice vector corresponds to the respective topmost layer, i.e., the lattice vector of graphene for the case of graphene/Ir(111) and the one of iridium for the case of clean Ir(111). Hence, the umklapp process happens within the topmost layer. The dark lines are most pronounced for wavelengths of the electron that lead to an approximate coincidence of the extremal amplitudes of the electron density wave traveling parallel to the surface with the atomic positions of the surface lattice. This fact suggests that the electron in this state still feels the corrugation of the local potential although it travels within the surface potential barrier close to the vacuum region. Hence, beyond the simple model of a surface barrier depending exclusively on the coordinate perpendicular to the surface plane, the lateral variation of the potential must be taken into account. In view of the fact that the discussed diffraction model does not require material-specific electronic properties except for the lattice parameters and excitation energy range, our observation suggests a general occurrence of the described interference patterns. While their specific intensity profile will certainly depend on the reflection and absorption coefficients, the position of the circular arcs exclusively depends on the lattice structure of the topmost atomic layer. The dark lines thus open a way of gaining precise structural data of the surface layer from low-energy photoemission data.

ACKNOWLEDGMENTS

We would like to thank the staff of BESSY for good support and Bene Poelsema, University of Twente (NL), for fruitful discussions. Funding by BMBF (Grant No. 05K16UMC) and Mainz Graduate School of Excellence is gratefully acknowledged.

[1] B. Poelsema, M. S. Altman, R. Van Gastel, H. J. W. Zandvliet, and A. Van Houselt, Ordinary and supernumerary resonant scattering of low energy electrons from the BiCu2 (111) surface alloy, New J. Phys. **19**, 013024 (2017).

[2] A. Winkelmann, M. Ellguth, C. Tusche, A. A. Ünal, J. Henk, and J. Kirschner, Momentum-resolved photoelectron interference in crystal surface barrier scattering, Phys. Rev. B **86**, 085427 (2012).

[3] Y. Zhu, S. Murali, W. Cai, X. Li, J. W. Suk, J. R. Potts, and R. S. Ruoff, Graphene-based Materials: Graphene and graphene oxide: Synthesis, properties, and applications, Adv. Mater. **22**, 3906 (2010).

[4] I. I. Klimovskikh, S. S. Tsirkin, A. G. Rybkin, A. A. Rybkina, M. V. Filianina, E. V. Zhizhin, E. V. Chulkov, and A. M. Shikin, Nontrivial spin structure of graphene on Pt(111) at the Fermi level due to spin-dependent hybridization, Phys. Rev. B **90**, 235431 (2014).

[5] K. S. Novoselov, D. Jiang, F. Schedin, T. J. Booth, V. V. Khotkevich, S. V Morozov, and A. K. Geim, Two-dimensional atomic crystals., Proc. Natl. Acad. Sci. USA **102**, 10451 (2005).

[6] E. Rotenberg and A. Bostwick, Superlattice effects in graphene on SiC(0001) and Ir(111) probed by ARPES, Synth. Met. **210**, 85 (2015).

[7] A. Varykhalov, J. Sánchez-Barriga, A. M. Shikin, C. Biswas, E. Vescovo, A. Rybkin, D. Marchenko, and O. Rader, Electronic and Magnetic Properties of Quasifreestanding Graphene on Ni, Phys. Rev. Lett. **101**, 157601 (2008).

[8] I. Pletikosić, M. Kralj, P. Pervan, R. Brako, J. Coraux, A. T. N'Diaye, C. Busse, and T. Michely, Dirac Cones and Minigaps for Graphene on Ir(111), Phys. Rev. Lett. **102**, 056808 (2009).

[9] M. Kralj, I. Pletikosić, M. Petrović, P. Pervan, M. Milun, A. T. N'Diaye, C. Busse, T. Michely, J. Fujii, and I. Vobornik, Graphene on Ir(111) characterized by angle-resolved photoemission, Phys. Rev. B **84**, 075427 (2011).

[10] C. Tusche, P. Goslawski, D. Kutnyakhov, M. Ellguth, K. Medjanik, H. J. Elmers, S. Chernov, D. Engel, A. Jankowiak, and G. Sch, Multi-MHz time-of-flight electronic bandstructure imaging of graphene on Ir (111), Appl. Phys. Lett. **108**, 261602 (2016).

[11] A. Adnot and J. D. Carette, High-Resolution Study of Low-Energy-Electron Diffraction Threshold Effects on W(001) Surface, Phys. Rev. Lett. **38**, 1084 (1977).

[12] E. G. McRae, Surface-state resonances in low-energy electron diffraction, Surf. Sci. **25**, 491 (1971).

[13] J. C. Le Bossé, J. Lopez, C. Gaubert, Y. Gauthier, and R. Baudoing, A general picture of threshold effects in LEED, J. Phys. C: Solid State Phys. **15**, 6087 (1982).

[14] Y. Gaubert, C. Baudoing, and R. Gauthier, General aspects of beam threshold effects in LEED, Surf. Sci. **147**, 162 (1984).

[15] A. T. N'Diaye, J. Coraux, T. N. Plasa, C. Busse, and T. Michely, Structure of epitaxial graphene on Ir(111), New J. Phys. **10**, 043033 (2008).

[16] H. Hattab, A. T. N'Diaye, D. Wall, G. Jnawali, J. Coraux, C. Busse, R. Van Gastel, B. Poelsema, T. Michely, F. J. Meyer Zu Heringdorf, and M. Horn-Von Hoegen, Growth temperature dependent graphene alignment on Ir(111), Appl. Phys. Lett. **98**, 141903 (2011).

[17] E. Loginova, S. Nie, K. Thürmer, N. C. Bartelt, and K. F. McCarty, Defects of graphene on Ir(111): Rotational domains and ridges, Phys. Rev. B: Condens. Matter Mater. Phys. **80**, 1 (2009).

[18] M. Mundschau, Emission microscopy and surface science, Ultramicroscopy **36**, 29 (1991).

[19] A. Oelsner, O. Schmidt, M. Schicketanz, M. Klais, G. Schönhense, V. Mergel, O. Jagutzki, and H. Schmidt-Böcking, Microspectroscopy and imaging using a delay line detector in time-of-flight photoemission microscopy, Rev. Sci. Instrum. **72**, 3968 (2001).

[20] G. Schönhense, K. Medjanik, and H.-J. Elmers, Space-, time- and spin-resolved photoemission, J. Electron Spectrosc. Relat. Phenomena **200**, 94 (2015).

[21] N. A. Cherepkov and G. Schönhense, Linear dichroism in photoemission from oriented molecules, Europhys. Lett. **24**, 79 (1993).

[22] E. Starodub, A. Bostwick, L. Moreschini, S. Nie, F. El Gabaly, K. F. McCarty, and E. Rotenberg, In-plane orientation effects on the electronic structure, stability, and Raman scattering of monolayer graphene on Ir(111), Phys. Rev. B **83**, 125428 (2011).

[23] S. Reich, J. Maultzsch, C. Thomsen, and P. Ordejón, Tight-binding description of graphene, Phys. Rev. B **66**, 035412 (2002).

[24] P. Eckerlin and H. Kandler, *Landolt-Börnstein: Numerical Data and Functional Relationships in Science and Technology* - New Series, Vol. 6 (Springer, Berlin, 1971).

[25] N. J. Speer, S.-J. Tang, T. Miller, and T.-C. Chiang, Coherent electronic fringe structure in incommensurate silver-silicon quantum wells, Science **314**, 804 (2006).

[26] D. Usachov, A. Fedorov, O. Vilkov, V. K. Adamchuk, L. V. Yashina, L. Bondarenko, A. A. Saranin, A. Grüneis, and D. V. Vyalikh, Experimental and computational insight into the properties of the lattice-mismatched structures: Monolayers of h-BN and graphene on Ir(111), Phys. Rev. B **86**, 155151 (2012).

[27] J. Sánchez-Barriga, A. Varykhalov, D. Marchenko, M. R. Scholz, and O. Rader, Minigap isotropy and broken chirality in graphene with periodic corrugation enhanced by cluster superlattices, Phys. Rev. B **85**, 201413 (2012).